Published in Composites Part A 2015, 73, 132-142

Compressive failure of laminates containing an embedded wrinkle; experimental and numerical study

Supratik Mukhopadhyay*, Mike I. Jones, Stephen R. Hallett

University of Bristol, Advanced Composites Centre for Innovation and Science, Queens Building, Bristol BS8 1TR, United Kingdom

*Corresponding author. Email: s.mukhopadhyay@bristol.ac.uk

Abstract

An experimental and numerical study has been carried out to understand and predict the compressive failure performance of quasi-isotropic carbon-epoxy laminates with out-of-plane wrinkle defects. Test coupons with artificially induced fibre-wrinkling of varied severity were manufactured and tested. The wrinkles were seen to significantly reduce the pristine compressive strength of the laminates. High-speed video of the gauge section was taken during the test, which showed extensive damage localisation in the wrinkle region. 3D finite element (FE) simulations were carried out in Abaqus/Explicit with continuum damage and cohesive zone models incorporated to predict failure. The FE analyses captured the locations of damage and failure stress levels very well for a range of different wrinkle configurations. At lower wrinkle severities, the analyses predicted a failure mode of compressive fibre-failure, which changed to delamination at higher wrinkle angles. This was confirmed by the tests.

Keywords: A. Carbon fibre B. Defects, Fracture C. Finite element analysis (FEA)

1 Introduction

The influence of manufacturing defects in laminated composites is an active area of research ([1,2]) due to their detrimental effect of final part quality. The most commonly found defects include voidage/porosity, in and out-of-plane fibre misalignment, local variations in fibre-volume fraction, fibre-resin debonds etc. Under mechanical loading, the overall failure of a structure is significantly influenced by the presence of such defects. Hence, it is crucial to accurately estimate the role of defects on the mechanical performance of composite structures in order to have a damage tolerant design. Out-of-plane misalignment of fibres is a type of defect also known as "wrinkling" [3]. Wrinkles are very commonly found in thick section components or curved composite parts as localised band of wavy fibres through-the-thickness. Geometric parameters such as amplitude, wavelength and waviness angle [4] are used to quantify the severity of the wrinkle. An example of a wrinkle defect occurring in a curved composite part is shown in Fig. 1(a).

The presence of wrinkles is known to reduce the compressive strength of composites [4–8]. Adams and Hyer [4] performed static compression tests on symmetric cross-ply laminates containing artificially produced embedded wrinkles of varied severity. For high-severity wrinkles, failure was found to be localised in the region of the wave. They found a reduction of compressive strength as high as 36% compared to pristine laminates. Post-test visual inspection revealed extensive through-the-thickness matrix cracking and delamination between plies in the failed specimens. Wisnom and Atkinson [9] carried out tests and FE analysis of compressive failure of unidirectional laminates with artificially induced waviness. They found from the analysis that fibre failure was triggered in the region of maximum misalignment and this was due to shear instability rather than the well-known classical

compressive instability. It was also noticed that the shear instability was essentially due to the shear non-linearity in the material response. Bradley et al [5] studied interlaminar strain localisation and compressive failure in two different types of wrinkle formation, namely a single wavy layer and three nested wavy layers located along the middle of cross-ply laminates. High normal and shear strains in the region of wrinkles were found using optical interferometry. The nested layer waves were seen to be approximately three times more severe in causing failure compared to the single layer wave. The predicted failures from FE models were less accurate when compared with test results. The authors concluded that simple stress based failure criteria may not be accurate in this case and identified the need for an improved formulation for failure prediction. Following the experimental work by Wang et al [8] to assess compressive failure in laminates containing waviness induced by ply-drops, Lemanski et al [6] did a numerical study with the same test configurations. The damage in the plies was approximated by a perfectly-plastic response while delamination between plies was modelled using cohesive elements in a 2D plane-stress framework. The test failure loads and the locations of damage in the failed test specimen compared well with the model results. However, it was acknowledged that 3D failure criteria for CFRP instead of a simple elastic-plastic material model may provide more accurate predictions in a general loading scenario. Leong et al [7] investigated compression failure in GFRP sandwich structures with wrinkles present in the face-sheet of sandwich panels. The damage initiated as a debonding between the face-sheet and core, localised at the wrinkle, which was followed by delamination in the face-sheet. The DIC strain contours near the wrinkle compared well with their FE analysis. The local failure initiation stresses predicted in the model by the Northwestern University (NU) criterion [10] correlated well with the tests. However, in absence of a progressive failure criterion, the global failure could not be successfully captured.

In the present work, a quasi-isotropic layup was chosen for study as this was more representative of layups used in industrial practice. Compared to uni-directional and cross-ply laminates, the compression failure behaviour in this case was more complex due to multiple active damage mechanisms and their interaction. Instead of visually inspecting the failed specimens to find out the failure modes, the progressive damage in the laminates was monitored by recording images at a very high frame rate during tests using a high-speed video camera. The information obtained from the tests was used to implement three-dimensional failure criteria at the inter-ply and intra-ply levels in a finite element framework. The FE results successfully captured the initiation of multiple interacting damage modes near the wrinkle and the progressive failure behaviour, which resulted in accurate prediction of failure stress levels. Previous work by the authors has looked at tensile loading of similar specimens [11] and here the experiments and models have been extended to compressive loading and predictions. The organisation of the paper is as follows: In Section 2, techniques for manufacturing and testing laminates containing artificially induced wrinkles of controlled severity are briefly described. The three dimensional FE models with the damage formulations are presented in Section 3. Section 4 discusses the findings from the tests and the results obtained from the models drawing a comparison between the two. Finally, in Section 5 conclusions are drawn based on the above study.

2 Experimental techniques

2.1 Wrinkle coupon manufacture

Hexcel's IM7/8552 pre-preg tape with a nominal cured ply thickness 0.125 mm was hand-laid to make quasi-isotropic ($[+45_2/90_2/-45_2/0_2]_{3s}$) compression test specimens with embedded wrinkles. The specimen dimensions were 110mm×30mm×6mm with a 30mm gauge length after tabbing. Test specimens of the same dimensions, free of any wrinkle, were

also manufactured to serve as a reference against which the wrinkle containing coupons were compared for compressive strength reduction. During the lay-up process, narrow 90° ply strips were introduced on already laid-up full-length 90° plies in certain locations which intentionally induced out-of-plane fibre wrinkle formation [8,11]. The severity of the wrinkle can be controlled by varying the width and thickness of the inserted strips (see Fig. 1(b)). Three distinct levels of wrinkle severities were produced by this method. Those were named level#1, level#2 and level#3 respectively, with a higher number representing a higher wrinkle angle. Eight test coupons for each of the three severity levels were manufactured. The wrinkle severities were estimated by taking images of the wavy-sections in the coupons and measuring the angle that a tangent drawn at a wavy ply made with a straight reference ply (see Fig. 2(a)). The average of the measured waviness angles for the level#1,2 and 3 specimens were 5.6°,9.9° and 11.4° respectively.

2.2 Compression testing

Uniaxial compression tests were performed on the coupons using the Imperial College compression test fixture [12] (see Fig. 2(b)) in a servo-hydraulic machine of 250kN capacity at a constant loading rate of 0.25 mm/min. Although no anti-buckling guides were used during the tests, preliminary FE analyses were carried out to confirm that the cross-sectional stress required to initiate buckling was higher than the mean compressive strength of the wrinkle-free baseline specimens. Because compressive failure is sudden and catastrophic in nature, a Photron SA-1 high-speed video camera was used to better understand the sequence of failure events. The camera was aimed at the edge of the gauge section during the test and used to take pictures at a frame rate of ~70000 frames/second. The load-displacement response as well as the data obtained from the video camera were later analysed to identify the initiation and interaction of different damage mechanisms.

3 Finite element modelling

3.1 Mesh generation

3D FE models of the laminates were built in Abaqus/Explicit [13]. Progressive failure behaviour was included in the models (discussed in the next section), which is known to cause convergence difficulties when an implicit solver is used. To overcome this, an explicit dynamic solver (but still with quasi-static loading rates) was used in this study. Selective mass scaling was used to ensure a reasonable time step size, while keeping its effect at a minimum to avoid spurious stress oscillations and dynamic effects in the solution. The plies were modelled using 8-noded solid C3D8R elements with one element through-the-thickness per ply. Layers of cohesive interface elements COH3D8 with zero thickness were inserted between ply elements to model delamination failure. To prevent spurious zero-energy hourglass modes in the reduced integration C3D8R elements, the "enhanced" hourglass control option available in Abaqus/Explicit was used. A fine mesh with in-plane dimension ~0.25mm×0.25mm was maintained in the location of the wrinkle and towards the laminate edges (where delaminations initiated first), while a comparatively coarser mesh was used elsewhere for computational efficiency (Fig. 3). A typical FE model of the compression specimen consisted of approximately 255,000 C3D8R elements and 140,000 COH3D8 elements. The wrinkle was approximated in the model as for the tension case [11] using a cosine function This function modified the through-thickness coordinates of a wrinkle-free uniform mesh with the help of a pre-processor MATLAB script using the expression:

$$h_w = h_0 + \Delta h \tag{1}$$

where h_w is the through-thickness nodal coordinate in the wrinkled configuration whereas h_0 is the corresponding value in a wrinkle-free flat laminate. The parameter Δh follows a sinusoidal waviness as follows:

$$\Delta h = \begin{cases} \frac{B\delta}{2}\cos(\frac{2\pi x}{\lambda}) & \text{if } -\frac{\lambda}{2} \le x \le \frac{\lambda}{2} \\ 0 & \text{otherwise} \end{cases} \quad (2)$$

where x is the dimension along the length of the laminate, λ is the wavelength of the wrinkle, δ is the amplitude of the wave and B is the variation of amplitude through-the-thickness. The value of B is unity on the centreline and reduces linearly through the thickness to zero at the surface. With this approximation, the maximum waviness angle θ can be analytically deduced:

$$\theta = \tan^{-1}\left(\frac{\pi\delta}{\lambda}\right) \quad (3)$$

In Eq. (3), δ and λ are the amplitude and wavelength of the wrinkle respectively. These parameters were directly measured from images of the wrinkle test coupons taken in microscope and fed into the mesh generation script for wrinkle FE models. In Fig. 4, the as manufactured laminates with three different grades of wrinkle severities and their corresponding FE meshes are shown. Also, Fig 5 draws comparison between wrinkle angles obtained by the cosine approximation in the model with the angle obtained directly from images by drawing a tangent to the wrinkled ply as described in Section 2.1.

3.2 Constitutive law

The mechanical constitutive behaviour of ply and cohesive elements were coded as VUMAT subroutines in Abaqus/Explicit. The following section gives brief description of these formulations.

3.2.1 Undamaged material response

The baseline formulation for the ply elements follows a 3D thermo-elastic orthotropic response. However, it is well known that composites behave non-linearly in shear in the in-plane and through-thickness directions. Makeev et al [14] have observed that nonlinear shear behaviour can be crucial for failure prediction of laminates containing wrinkle defects, depending upon the specific lay-up chosen for study. For this reason, a non-linear shear stress-strain relation of the following form was assumed in these two directions:

$$\sigma_{1i} = \mathrm{sgn}(\gamma_{1i})(A(1-\mathrm{e}^{-B|\gamma_{1i}|})) \qquad i = 2,3 \tag{4}$$

In Eq. (4), σ_{ij} and γ_{1i} are shear stress and engineering shear strain respectively. The numeric indices in Eq. (2) denote the ply principal directions. The parameters *A* and *B* are obtained by least-square fit to the experimental data. In this work A and B were found to be 145 and 38 by fitting to the data given for IM7/8552 in [14]. Although the loading part in 1-3 and 1-2 directions were considered non-linear, the unloading was linear following the initial slope of the load curve. The elastic stiffness values for IM7/8552 used in this work are reported in Table 1.

3.2.2 Matrix cracking under transverse compression

The continuum damage model for matrix failure under transverse compression used here follows Pinho et al. [15]. The material parameters used for this model are given in Table 2. This model builds upon Puck's theory [16] which assumes a crack plane oriented at a certain angle φ to the ply normal before failure (Fig. 6(a)). In the models, the orientation of the crack plane was determined by iterating between 0° and 180° at discrete angular intervals of 5° and maximising a suitable failure criterion. In compression, the following criterion was used:

$$\left(\frac{\tau_T}{S_T-\mu_T\sigma_N}\right)^2+\left(\frac{\tau_L}{S_L-\mu_L\sigma_N}\right)^2=1 \tag{5}$$

In Eq. (5), σ_N, τ_T and τ_L are respectively the normal and two shear direction traction components on the crack plane. S_T and S_L are the transverse and longitudinal matrix shear strengths respectively, while μ_T and μ_L are the corresponding friction coefficients. S_T can be obtained from the transverse compressive strength Y_c following the procedure given in [17]. Although Eq. (5) was evaluated on multiple 2D planes, the normal and shear traction components on each plane were derived by transforming the six stress components in the lamina frame to each of these planes. Therefore, this formulation is fully 3D in nature.

Once the failure criterion (Eq. (5)) was satisfied, a resultant shear stress τ^{mat} was derived and an effective stress σ^{mat} on the crack plane was calculated:

$$\tau^{mat}=\sqrt{\tau_T^2+\tau_L^2} \tag{6}$$

$$\sigma^{mat}=\sqrt{\langle\sigma\rangle_n^2+\left(\tau^{mat}\right)^2} \tag{7}$$

The superscript "mat" indicates quantities related to the matrix cracking model. The Macaulay bracket on σ_N indicates that negative normal traction component does not contribute to effective stress, as it tends to close any cracks. An effective fracture energy G_{eff} based on the present mode mixity was also deduced following the power law criterion[18]:

$$\left(\frac{G_I}{G_{Ic}}\right)^{\alpha}+\left(\frac{G_{II}}{G_{IIc}}\right)^{\alpha}=1 \tag{8}$$

Here G_I and G_{II} are the mode I and mode II energy release rates, the subscript 'c' denotes the corresponding critical energy release rates and α is an exponent usually determined from

experimental mixed-mode data. An effective driving strain ε^{mat} on the crack plane was established as follows:

$$\gamma^{mat} = \left|\gamma_T \cos\beta + \gamma^{el}{}_L \sin\beta\right| \tag{9}$$

$$\varepsilon^{mat} = \frac{\langle\sigma_n\rangle}{\sigma_n}\varepsilon_n \sin\omega + \gamma^{mat}\cos\omega \tag{10}$$

where ε_n indicates normal strain and γ_T, $\gamma^{el}{}_L$ are the shear strains on the fracture plane which were obtained by projecting the global strains on the fracture plane. The Macaulay bracket on σ_n indicates that normal compression has no effect on driving strain. The superscript 'el' in Eq. (9) indicates only the elastic component of the in-plane shear strain participates in the fracture process. Referring to Fig. 6(b), β is the angle between τ^{mat} and τ_T, which is defined as $\beta = \tan^{-1}(\tau_L / \tau_T)$, while ω is the angle between σ^{mat} and τ^{mat}, defined by $\omega = \tan^{-1}(\sigma^{mat} / \tau^{mat})$. The angles β and ω define the direction of the effective stress σ^{mat} with respect to the fracture plane. These angles are used in Eq. (9) and (10) to orient ε^{mat} in the direction of σ^{mat} on the fracture plane.

At damage initiation, the driving strain was denoted by ε_0^{mat} and its value at complete failure was given by:

$$\varepsilon_f^{mat} = \frac{2G_{eff}}{\sigma_0^{mat} l_c} \tag{11}$$

In Eq. (11), σ_0^{mat} is the effective stress (given by Eq. 7) at the crack-plane at damage initiation and l_c is the characteristic length of the finite element. The characteristic length in Eq. (11) ensured mesh size independent energy dissipation at failure. A damage parameter $d \in [0,1]$ was also established as:

$$d = \max\left\{0, \min\left\{1, \frac{\varepsilon_f^{mat}(\varepsilon^{mat} - \varepsilon_0^{mat})}{\varepsilon^{mat}(\varepsilon_f^{mat} - \varepsilon_0^{mat})}\right\}\right\} \tag{12}$$

This damage parameter was used to degrade the traction components on the fracture plane to zero using a bilinear law (Fig. 6(c)).

3.2.3 Fibre kinking failure under axial compression

It is well known that high fibre volume-fraction composites fail in axial compression by the formation and broadening of a highly localised and strained zone called 'kink band'[19]. Due to initial fibre misalignments and manufacturing defects [20], the shear stress acting on the fibres during compression cause them to rotate further leading to kink band initiation and subsequent failure. Following the plane-stress based fibre-kinking model by Dávila et al [21], Pinho et al. formulated a fully three dimensional compressive fibre failure criterion [15,17]. This model was used in the present work, with Table 2 containing the material input parameters used. For completeness, a brief outline of the model is provided here and the reader is referred to [15] for more details.

The continuum damage model for fibre kinking assumes that the plane of kink-band formation has a general orientation and is not necessarily aligned with the *a*-*b* plane of the lamina coordinate system (see Fig. 7) in a three dimensional stress state. Considering this orientation to be a principal direction in the *b*-*c* plane [17], the angle ψ between the kink-plane and the *b* axis was calculated as:

$$\tan 2\psi = \frac{2\sigma_{bc}}{\sigma_b - \sigma_c} \tag{13}$$

Once the kink-plane was determined, the stresses in the material axes were rotated to this frame (coordinate system $a - b_\psi - c_\psi$ in Fig. 7). This model assumes that the fibres already have a small initial misalignment angle θ_i, due to which, any axial compression produces

shear parallel to fibres causing further fibre rotation. The final misalignment angle θ due to additional fibre rotation was found by:

$$\theta = \text{sgn}(\sigma_{ab_\psi})(\theta_i + \gamma_{mi}) \tag{14}$$

where γ_{mi} is the additional shear strain in the initial misalignment frame found using Eq. (4) from the knowledge of the corresponding shear stress in that frame. Next, the stresses in the $a - b_\psi - c_\psi$ frame were rotated to the final misalignment frame $a_m - b_m - c_\psi$. In this frame the transverse matrix failure criterion in compression was checked using Puck's criterion (Eq. (5)). Although the failure criterion was checked in a 2D misalignment frame, the orientation of this frame was determined from the six stress components on the lamina frame a-b-c (Fig. (7)). Therefore, similar to the matrix failure model, the fibre kinking model is also a 3D failure model.

Once failure was initiated, based on the user input for fibre fracture energy G_{kink}, an effective kink-band strain was formulated (which is basically the shear strain in the kink-band responsible for the fibre rotation) and its value at complete failure was determined from user input of fibre fracture energy G_{kink} and characteristic element length l_c similar to Eq. (11). A damage variable of similar form to Eq. (12) was introduced, which was a function of the effective kink-band strain. This was used to degrade the relevant kink-band stresses to zero at complete failure.

As seen from Eq. (14), this model required the knowledge of an initial misalignment angle θ_i. Initial fibre misalignments between 1°-2° are typical in fibre composite structures as found by Yurgartis [22]. In the present work, a misalignment of 1.5° was used for all the models. This was obtained by calibrating a model against the test results for the compression strength of wrinkle-free baseline laminates.

3.2.4 Delamination

Interfacial failure between plies was modelled using a 3D cohesive interface constitutive law [23] which is outlined here in brief. In the undamaged state, the opening (mode I) and sliding (mode II) displacements between the top and bottom surfaces of the cohesive element (see Fig. 8(a)) were related to the corresponding traction components by high stiffness values K_I and K_{II} [24]. A quadratic interaction between the traction components was used to detect damage initiation:

$$\sqrt{\left(\frac{\langle \sigma_{33} \rangle^2}{\sigma_{I\max}}\right)^2 + \left(\frac{\sqrt{{\sigma_{12}}^2 + {\sigma_{13}}^2}}{\sigma_{II\max}}\right)^2} = 1 \qquad (15)$$

In Eq. (15), σ_{33} indicates the traction component normal to the mid-plane of the cohesive element, while σ_{12} and σ_{13} are the shear traction components in the mid-plane of the element. $\sigma_{I\max}$ and $\sigma_{II\max}$ are the mode I and mode II failure initiation stresses. After failure was detected at the interface, Eq. (8) was used to find the mixed-mode fracture energy. Following this, an interfacial-displacement driven damage variable $d_{delam} \in [0,1]$ was formulated:

$$d_{delam} = \max\left\{0, \min\left\{1, \frac{\delta_m - \delta_m^e}{\delta_m^f - \delta_m^e}\right\}\right\} \qquad (15)$$

where δ_m is the effective interfacial mixed-mode displacement. The superscript '*e*' and '*f*' indicate its value corresponding to failure initiation and complete failure respectively. This damage variable d_{delam} was used to degrade the interfacial traction components linearly to zero at complete failure following a mixed-mode delamination map (Fig. 8(b)). The material parameters for this damage model are given in Table 3.

In the implementation for delamination, the top surfaces of the cohesive elements were collapsed on the bottom surfaces to have a zero thickness interfaces. Following the technique proposed by González et al [25], the strains given by the subroutine were converted to interfacial displacements which were then related to the traction components using the constitutive law.

4 Results

4.1 Test

4.1.1 Compressive strength reduction in wrinkle specimens

On average, six specimens were tested for both the baseline defect-free configuration and the three levels of wrinkle severities to ensure results were of statistical significance. In all the cases, the failure was catastrophic and accompanied by an audible noise. The cross-sectional stress levels of the pristine and the wrinkle specimens corresponding to complete failure are given in Table 4. It was seen that although the level#2 and level#3 configurations differed in terms of their respective wrinkle severities, their failure stress levels were comparable; both were lower than the mean pristine strength by ~ 34%. This clearly shows the influence of wrinkles to cause early knockdown in compressive strength. The extent of this knockdown is found to be in line to the observations of earlier researchers (e.g. Adams and Hyer [4] noted ~ 36% compressive strength reduction due to wrinkle on cross-ply laminates). Even the level#1 configuration with the lowest level of wrinkle severity of ~ 5.6°, was noted to reduce the pristine strength by 18%.

4.1.2 Failure mechanisms

Because of the sudden nature of failure, it was difficult to uniquely identify and isolate the interacting damage mechanisms. From the post-test visual inspection, it was confirmed that

the failure happened in the gauge section, being localized at the wrinkle and that there were multiple delaminations and fibre breakages through the thickness (Fig. 9). The high-speed imaging was important in this regard as it revealed much more information beyond this preliminary understanding. Fig. 10(a)-(d) shows successive frames of a typical level#1 specimen just at the point of failure, taken at 72,000 frames/second. As shown in Fig. 10(b), a fibre failure occurred first in one of the axial plies, which then unloaded by causing adjacent delaminations, cracks and fibre failure in other plies through-the-thickness (Fig. 10(c)-(d)). Four out of six level#1 specimens tested consistently showed this failure behaviour. The two remaining specimens of this grade of wrinkle severity failed at a lower load level compared to the others, and showed delamination occurring before fibre failure, as captured by the high-speed video. This failure mode is more consistent with the failure mode of higher wrinkle angles. It thus appears that this level #1 wrinkle angle is near the transition point in failure mode. This was confirmed by the modelling presented in Section 4.2.2 where, it was seen that for this configuration, ignoring the fibre failure mode in the model gave only a very small increase in failure load to delamination (~7%, see Fig 13(b)). Although all the specimens were extracted from the same panel, small variations from specimen to specimen in terms of both local wrinkle angle and material properties seem sufficient to bring the delamination load below that of fibre failure in a minority of cases. The higher wrinkle severity specimens (level#2 and 3) showed a completely different sequence of damage events than the majority of level#1 specimens. In Fig. 11(a)-(d), a typical level#3 specimen is shown failing, taken with a frame-rate of 67,500 frames/second. The first three frames (Fig. 11(a)-(c)) show the evolution of transverse matrix cracks and delaminations in the 90° plies in the wavy region which transferred the load to the axial plies. The axial plies finally failed by fibre compressive failure (Fig. 11(d)). This pattern of failure was consistently found in all the level#3 specimens tested. Although the wrinkle severity of the level#2 specimens were lower

(see Section 2.1) than the level#3 specimens, an almost identical sequence of damage evolution was observed in them, with delaminations and matrix cracks developing first, followed by fibre failure of the axial plies due to overloading. Hence, from the high-speed imagery it could be deduced that for lower wrinkle severity, fibre failure was the dominant failure mechanism while for the higher wrinkle severities, the failure was governed by delaminations and intra-laminar cracks which ultimately caused fibre failure.

4.2 Model

4.2.1 Prediction of failure stress levels

For all the FE models, a two-step analysis was performed. In the first step, the ambient temperature was linearly ramped down through a temperature difference of 160°C to simulate residual stress development due to cool-down from final cure temperature (180°C) to room temperature (20°C). Following this, velocity boundary conditions were applied on two ends of the specimen in opposite directions while keeping the ambient temperature constant. Fig 12(b) shows the cross-sectional failure stress predictions from the FE models compared against the test results. As can be seen, the model results in general match very well with the test data. However, the models predict slightly higher failure stress for level#2 wrinkle configuration than a level#3 configuration while in the test their failure stresses were found to be comparable (see Section 4.1.1). Nonetheless, the prediction errors for all the wrinkle severities were within 10%.

It should be noted that modelling the residual stress development in the laminate due to cure shrinkage, was crucial to predict the point of failure accurately in these cases. It was observed that neglecting this effect and considering only compression loading until the point of failure resulted in over prediction of the failure stress levels (see Fig. 12(a) for a representative example of a level#3 specimen).

4.2.2 Failure modes in the model

The failure in all the models was catastrophic in nature. The level#1wrinkle model was found to fail by fibre compression failure. In Fig. 13 (a), a frame is shown highlighting fibre failure in the axial plies in the wrinkle. This was followed shortly afterwards by extensive delamination in the model. To confirm that the leading damage mechanism in this case was indeed fibre failure, the model was run without this failure mode and considering only transverse compressive matrix cracking and delamination to cause failure of the structure. Fig. 13(b) shows that not incorporating fibre failure in the model over predicted the failure stress which clearly indicates that the delamination initiated later than fibre failure in the model and therefore fibre failure is the dominant mechanism for this level of wrinkle severity, as observed in the tests (see Section 4.1.2). Unlike level#1wrinkle, the more severe wrinkle configurations e.g. level#2 and 3 were found to be governed by inter-ply delamination (initiated due to localised through-thickness shear stress at the wrinkle) and intra-ply matrix cracking, similar to test findings. To illustrate this point, delamination development in the wavy region between 90°/45° plies in the level#3 specimen is shown in Fig. 14 (a) during failure. As observed in both the level#2 and 3 severity models, delamination in the wavy region caused catastrophic failure of the structure and fibre failure in these cases happened only after delamination, hence was not the driving mode of damage. As before, to confirm this assertion, the level#3 model was run with and without the fibre failure model. The results are shown in Fig. 14(b), which indicates no influence of fibre failure in this case. Exactly the same observation was made for the level#2 wrinkle configuration as well.

For the level#2 and 3 specimens, it was equally important to correctly capture the matrix cracking behaviour in the 90° plies because the cracks caused local load re-distribution and promoted delamination. In Fig. 15 (a)-(b), similar crack locations between test and model of

the level#3 specimen just before failure are compared. Although the majority of the matrix cracks seen are in the 90° plies, some unrealistic cracks also developed in the adjacent 45° plies, which could be a result of the dynamic effect due to the catastrophic delamination. However, these spurious effects did not have a major influence on the overall load-displacement response of the models.

Fig. 16 compares the damage initiation and progression for both delamination and fibre kinking failure (the major failure modes observed in tests) for all the three wrinkle severities Although, all of the 0° plies eventually predicted fibre failure, for clarity, only the two central 0° plies in the models are shown, where this failure mode was seen to initiate first. Fig. 16 clearly shows that the driving failure mode for level#1 is fibre failure, while for higher wrinkle severities, significant delamination has already initiated before any fibre damage to the axial plies, as also observed from tests.

4.2.3 Mesh sensitivity of results

As stated in Section 4.2.2, the failure mode of level#1 wrinkle configuration was fibre compressive failure while the level#2 and 3 wrinkle specimens were dominated by inter-ply delamination. Hence a mesh refinement study was done both for level#1 and level#3 specimens using three different mesh densities. The results presented in Section 4.2 are from the baseline model with 393,624 elements and a varied in-plane mesh density (see Fig. 3) with a finer mesh at the laminate edges and wrinkle (minimum element size 0.25×0.25mm) and a relatively coarser mesh elsewhere (maximum element size 0.75mm×0.25mm) for computational efficiency. Two other cases with uniform in-plane mesh densities were investigated: a mesh with 204,120 elements and element size 0.5 mm×0.5 mm. and another one with 554,000 elements and element size 0.3mm×0.3mm. In all cases, a single element through-the-thickness was used to model plies as well as cohesive interfaces. Cross-sectional

stress vs. displacement results for level#1 specimen (Fig. 17 (a)) for the three cases show negligible influence of the mesh size for the baseline model and the model with 0.3mm element length, while the model with element size 0.5 mm slightly overpredicted the failure initiation load due to a coarser mesh. Fig. 17(b) show the results for the level#3 specimens indicating no influence of element size on the overall failure process. In this case, the failure was dictated by delamination and the levels of mesh refinement for all the three cases gave a well formed cohesive zone ahead of the delamination front which resulted in mesh-independent response.

4.2.4 Wrinkle severity vs. failure stress

A parametric study was carried out to predict the effect of wrinkle severity on compression strength of the quasi-isotropic stacking configuration. Another objective of this study was to know the level of wrinkle severity at which the dominant mode of failure changed from fibre compression to delamination. For this purpose, FE models were developed with overall geometric dimensions remaining the same as in Fig. 3, but with the wrinkle severity varying from 1° to 10° in intervals of 1°. This was achieved by changing the amplitude of the wrinkle in the models while keeping the wavelength constant. The final failure predictions for this study, together with the test results of the three specific wrinkle levels tested, are shown in Fig. 18. The model results for the tested wrinkle angles are also plotted. It can be observed that a transition point between the two failure modes occurs between wrinkle angles of 8 and 9°. To the left of this transition, specimens predominantly failed by fibre failure (shown by blue circular markers) while to the right, the wrinkle severities were high enough to initiate delamination before fibre failure (shown by red square markers).

5 Conclusions

In this study, the effect of embedded fibre wrinkle defects on the compressive strength of multi-directional composite laminates was investigated experimentally and numerically. Contrary to the commonly followed approach of identifying failure modes from post-test visual inspection, high-speed video recording was employed during the tests, which revealed detailed information about the failure modes and their interaction in the region of the wrinkle during the very short time within which the specimen failed. Two distinct principal modes of failure were observed; fibre compressive failure as the dominant mechanism for lower severity wrinkles and inter-ply delamination for higher severity wrinkles. Detailed 3D FE models of the wrinkle specimens were built and run, incorporating all the failure modes observed experimentally via the implementation of user defined material models. The models predicted the failure load levels to with 10% of the mean test result for each severity and correctly determined the dominant failure mode and location for each case. The models were also used to generate predictions of compressive strength for a range of wrinkle severities, which clearly identified a threshold wrinkle configuration beyond which the dominant failure mechanism changed, consistent with experimental observations. The failure of higher severity wrinkles were dominated by delamination. The matrix cracking model was also useful in these cases, as it caused local load-redistribution during failure and helped to correctly capture the final failure stress levels in the FE models.

6 Acknowledgements

The authors would like to acknowledge Rolls-Royce plc for the support of this research through the Composites University Technology Centre (UTC) at the University of Bristol, UK.

7 References

[1] Potter KD. Understanding the origins of defects and variability in composites manufacture. 17 th International Conference on Composite Materials, Edinburgh International Convention Centre, Edinburgh, UK: 2009, pp. 27–31.

[2] Potter KD, Khan B, Wisnom M, Bell T, Stevens J. Variability, fibre waviness and misalignment in the determination of the properties of composite materials and structures. Composites Part A: Applied Science and Manufacturing 2008;39:1343–54.

[3] Bloom LD, Wang J, Potter KD. Damage progression and defect sensitivity: An experimental study of representative wrinkles in tension. Composites Part B: Engineering 2013;45:449–58.

[4] Adams DO, Hyer M. Effect of layer waviness on the compression strength of thermoplastic composite laminates. Journal of Reinforced Plastics and Composites 1993;12:414–29.

[5] Bradley D., Adams D., Gascoigne H. Interlaminar strains and compressive strength reduction due to nested layer waviness in composite laminates. Journal of Reinforced Plastics and Composites 1998;17:989–1011.

[6] Lemanski SL, Wang J, Sutcliffe MPF, Potter KD, Wisnom MR. Modelling failure of composite specimens with defects under compression loading. Composites Part A: Applied Science and Manufacturing 2013;48:26–36.

[7] Leong M, Overgaard LCT, Thomsen OT, Lund E, Daniel IM. Investigation of failure mechanisms in GFRP sandwich structures with face sheet wrinkle defects used for wind turbine blades. Composite Structures 2012;94:768–78.

[8] Wang J, Potter K, Hazra K, Wisnom M. Experimental fabrication and characterization of out-of-plane fiber waviness in continuous fiber-reinforced composites. Journal of Composite Materials 2011;46:2041–53.

[9] Wisnom MR, Atkinson JW. Compressive failure due to shear instability : Experimental investigation of waviness and Correlation with Analysis. Journal of Reinforced Plastics and Composites 1996;15:420–39.

[10] Daniel IM, Luo J-J, Schubel PM, Werner BT. Interfiber/interlaminar failure of composites under multi-axial states of stress. Composites Science and Technology 2009;69:764–71.

[11] Mukhopadhyay S, Jones MI, Hallett SR. Static tensile failure of composite laminates containing an embedded wrinkle; numerical and experimental study. Submitted 2014.

[12] Matthews FL, Haberle J. A new method for compression testing. European Conference on Composites Testing And Standardisation, Amsterdam, Netherlands: 1992, pp. 91–9.

[13] Abaqus Inc. Abaqus 6.12 users manual. Providense,RI,USA: 2012.

[14] Makeev A., Seon G, Lee E. Failure Predictions for Carbon/Epoxy Tape Laminates with Wavy Plies. Journal of Composite Materials 2009;44:95–112.

[15] Pinho ST, Iannucci L, Robinson P. Physically based failure models and criteria for laminated fibre-reinforced composites with emphasis on fibre kinking. Part II: FE implementation. Composites Part A: Applied Science and Manufacturing 2006;37:766–77.

[16] Puck A, Schurmann H. Failure analysis of FRP laminates by means of physically based phenomenological models. Composites Science and Technology 1998;3538:1045–67.

[17] Pinho ST, Iannucci L, Robinson P. Physically-based failure models and criteria for laminated fibre-reinforced composites with emphasis on fibre kinking: Part I: Development. Composites Part A: Applied Science and Manufacturing 2006;37:63–73.

[18] Mi Y, Crisfield MA, Davies GAO, Hellweg HB. Progressive Delamination Using Interface Elements. Journal of Composite Materials 1998;32:1246–72.

[19] Lee J, Soutis C. A study on the compressive strength of thick carbon fibre–epoxy laminates. Composites Science and Technology 2007;67:2015–26.

[20] Argon A. Fracture of composites. Treatise on Materials Science and Technology 1972;1:79–114.

[21] Dávila CG, Camanho PP. Failure Criteria for FRP Laminates in Plane Stress. Tech. Rep. NASA/TM-2003-212663. National Aeronautics and Space Administration. 2003.

[22] Yurgartis SW. Measurement of small angle fiber misalignments in continuous fiber composites. Composites Science and Technology 1987;30:279–93.

[23] Jiang WG, Hallett SR, Green BG, Wisnom MR. A concise interface constitutive law for analysis of delamination and splitting in composite materials and its application to scaled notched tensile specimens. International Journal for Numerical Methods in Engineering 2007;69:1982–95.

[24] Harper PW, Hallett SR. Cohesive zone length in numerical simulations of composite delamination. Engineering Fracture Mechanics 2008;75:4774–92.

[25] González EV, Maimí P, Turon A, Camanho PP, Renart J. Simulation of delamination by means of cohesive elements using an explicit finite element code. Computers, Materials and Continua 2009;9:51–92.

Figures

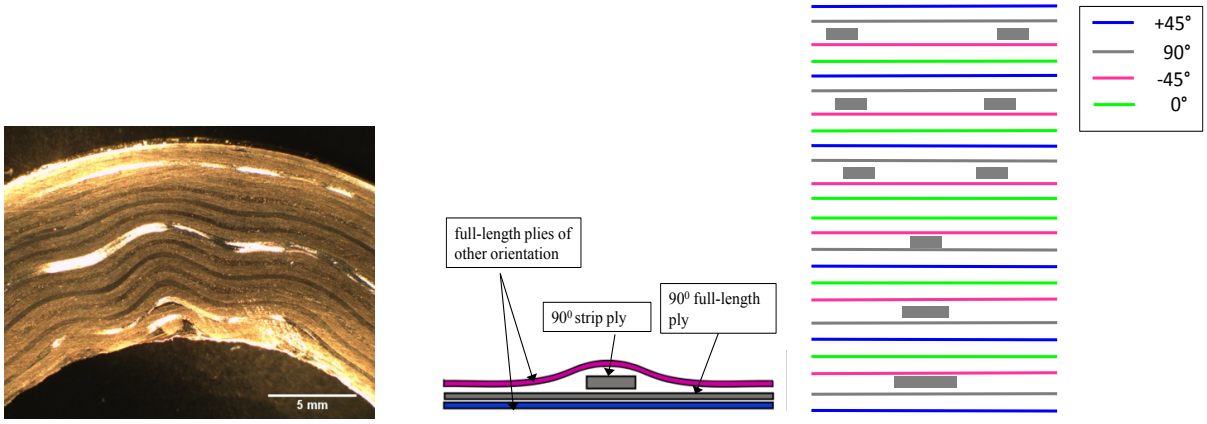

(a) (b)

Figure 1. (a)Wrinkle formation in a curved composite part. (b) Lay-up profile of the laminate showing the location of inserted strips.

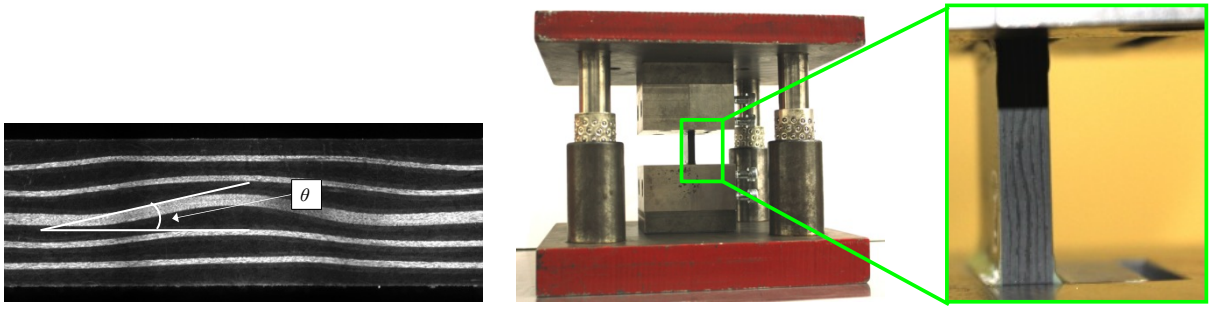

(a) (b)

Figure 2. (a) Measurement of wrinkle angle by tangent drawing technique. (b) ICSTM compression test fixture showing wrinkle specimen held between clamping blocks

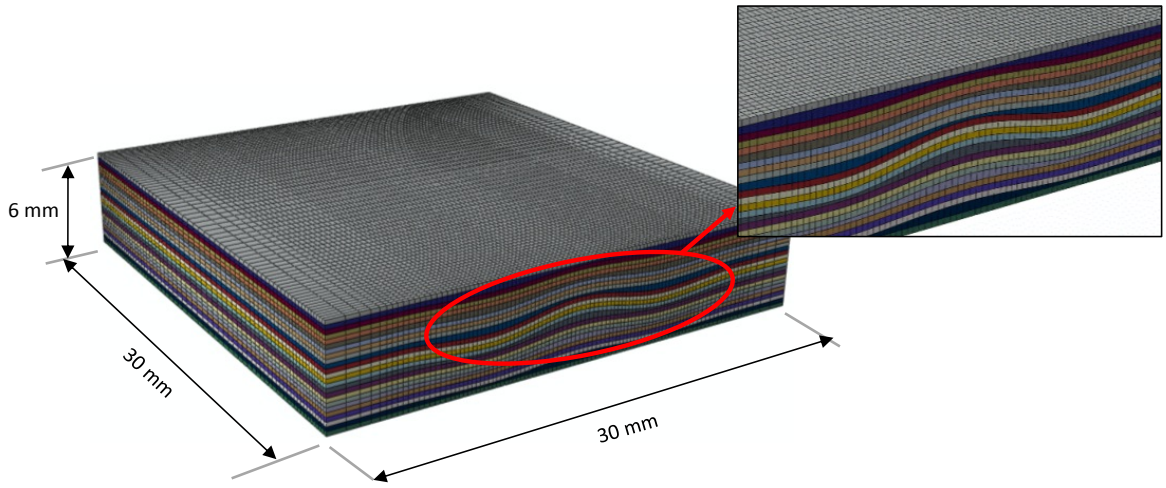

Figure 3. FE mesh of the wrinkle specimen highlighting the wrinkle region developed using cosine approximation. Thickness variation in 90° plies (due to insertion of strips in test) is captured accurately.

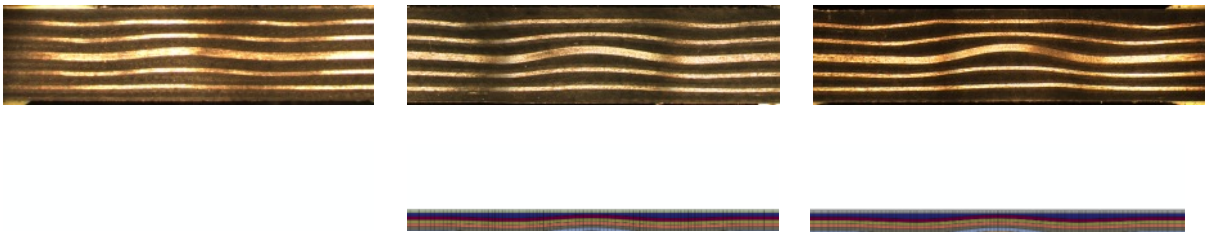

(a) (b) (c)

Figure 4. The three levels of wrinkle severities (a) Level. #1 (b) Level #2 (c) Level #3 showing as manufactured test specimens (above) and their corresponding FE realisations (below).

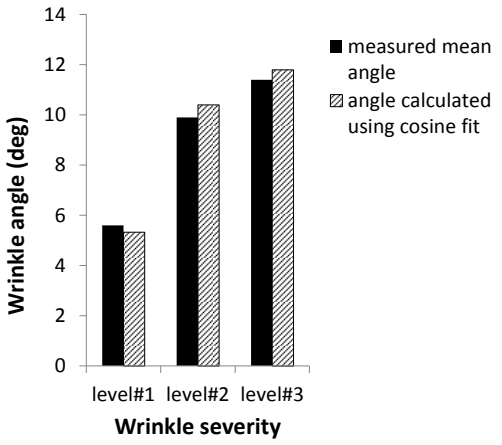

Figure 5. Comparison of wrinkle angle measured by tangent drawing technique and angle calculated using measured amplitude and wavelength and fitting to a cosine curve.

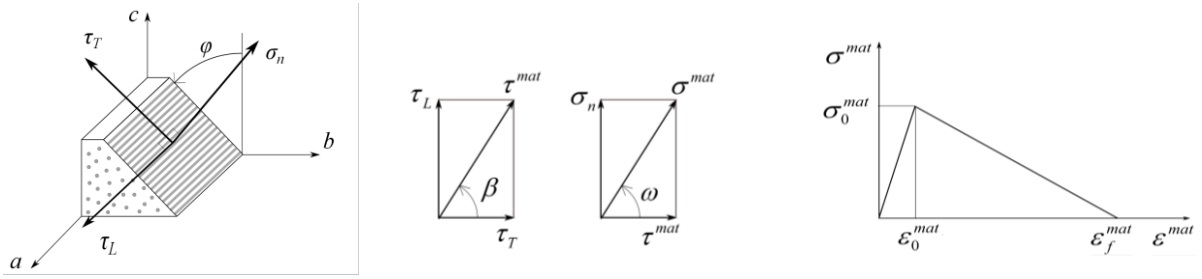

(a) (b) (c)

Figure 6. (a) Traction components on the matrix fracture plane. (b) Definition of angles on the fracture plane. (c) Bilinear damage propagation law, redrawn after [16]

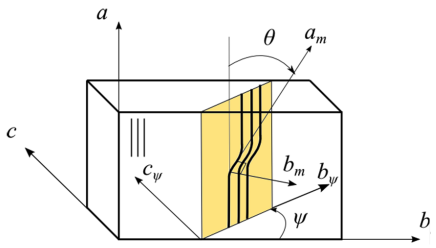

Figure 7. Fibre kinking model showing the kink plane and fibre-misalignment frame with respect to the a-b-c lamina co-ordinate system, redrawn after [16].

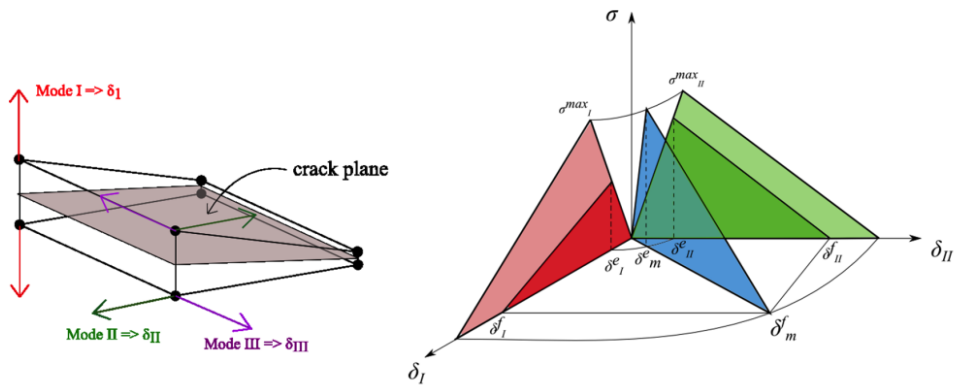

(a) (b)

Figure 8. (a) Interfacial relative displacements in a cohesive element. (b) Mixed mode delamination map, redrawn after [22]

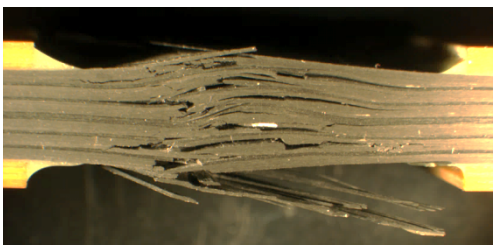

Figure 9. A typical failed specimen showing multiple fibre breakage and delamination through-the-thickness.

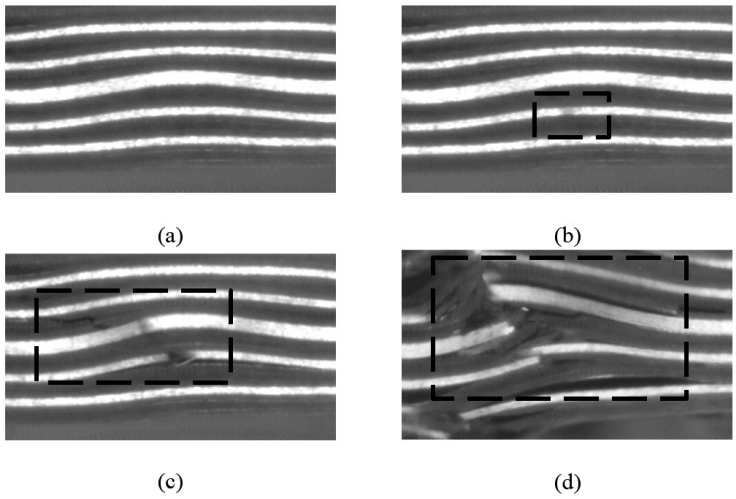

Figure 10. High-speed camera images of damage sequence in a level#1 specimen.(a) just prior to damage. (b) fibre failure in axial ply.(c)-(d) further fibre failure and delamination through-the-thickness

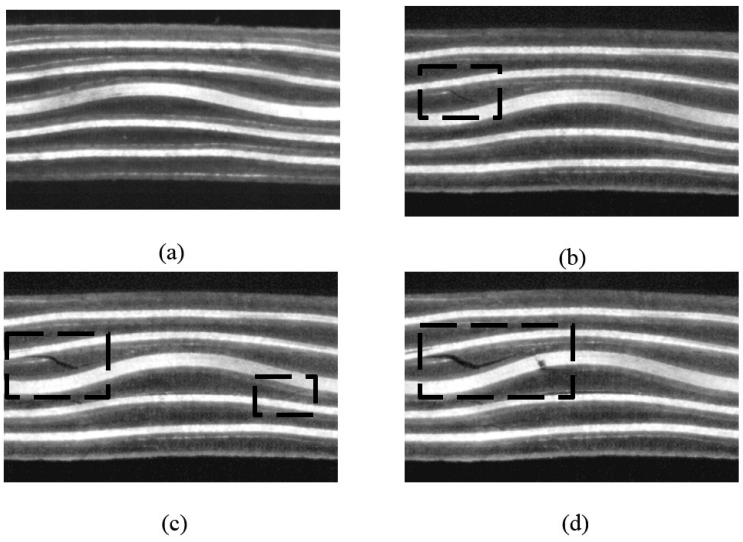

Figure 11. High-speed camera images of damage sequence in a level#3 specimen.(a) just prior to damage. (b)-(c) shows evolution of matrix cracks and delamination in 90° plies which overloads axial plies. (d) fibre failure

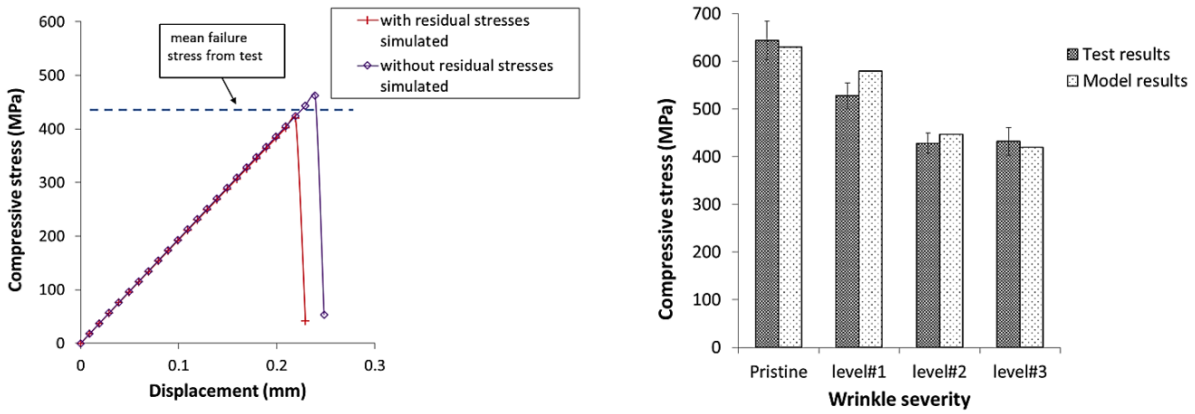

(a) (b)

Figure 12. (a) Failure stress obtained from model of a level #3 specimen with and without including residual stress development due to cure shrinkage. (b) Comparison of compressive strengths of the three levels of wrinkle specimens from tests and model.

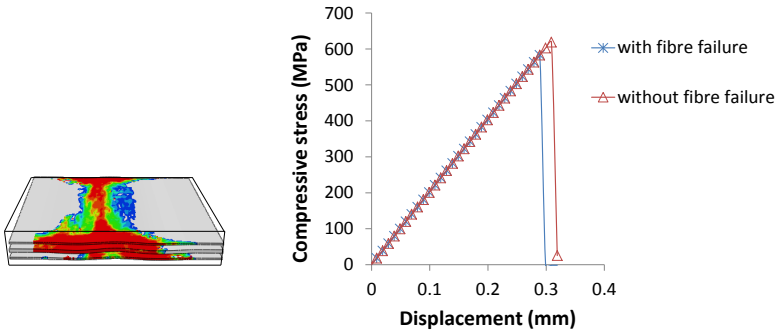

(a) (b)

Figure 13. (a) Fibre kinking failure (shown in red) in the 0° plies in level#1 wrinkle model (upper 0° ply removed for clarity). (b) Failure stress with and without including fibre failure showing over prediction in the latter case

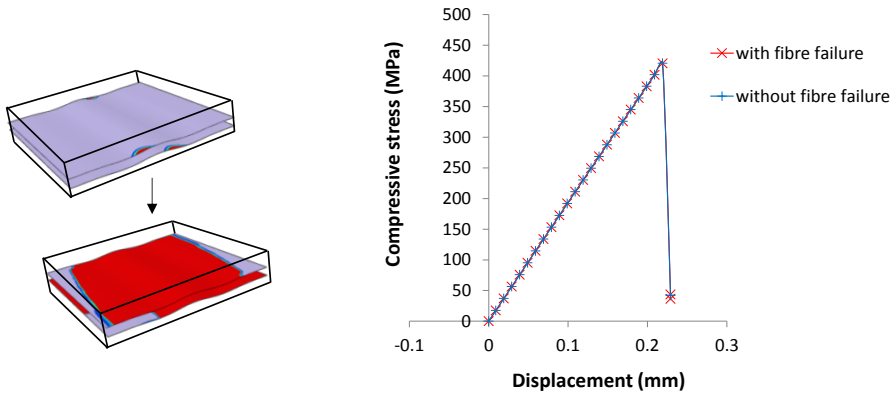

(a) (b)

Figure 14. (a) Two successive frames of the FE analysis of level#3 specimen model showing catastrophic delamination in 45°/90° cohesive layers leading to sudden failure (failed elements shown in red). (b)Model run with and without fibre failure mode, indicating no influence of fibre failure in this case.

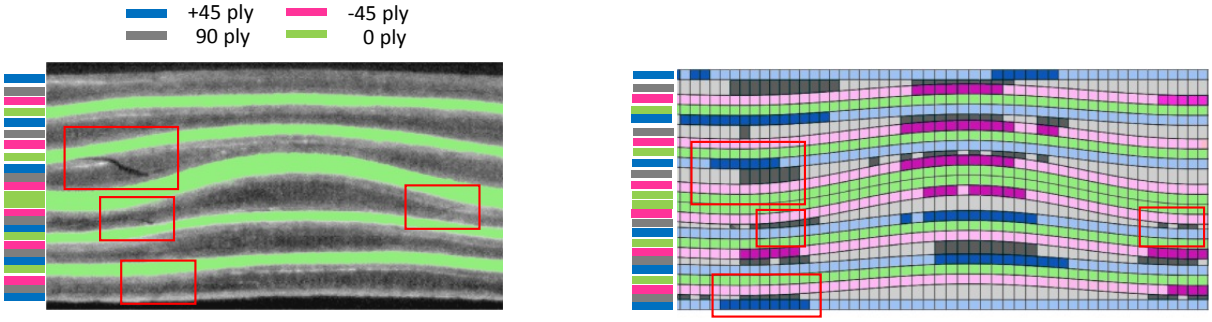

(a) (b)

Figure 15. Comparison between similar matrix crack locations just before failure in (a) test and in (b) model for a level#3 wrinkle severity. Colour coding is used to identify plies of different orientation. In (a), the 0° plies are shaded in green. In (b), the corresponding darker shades of colour in each ply denote the damaged locations.

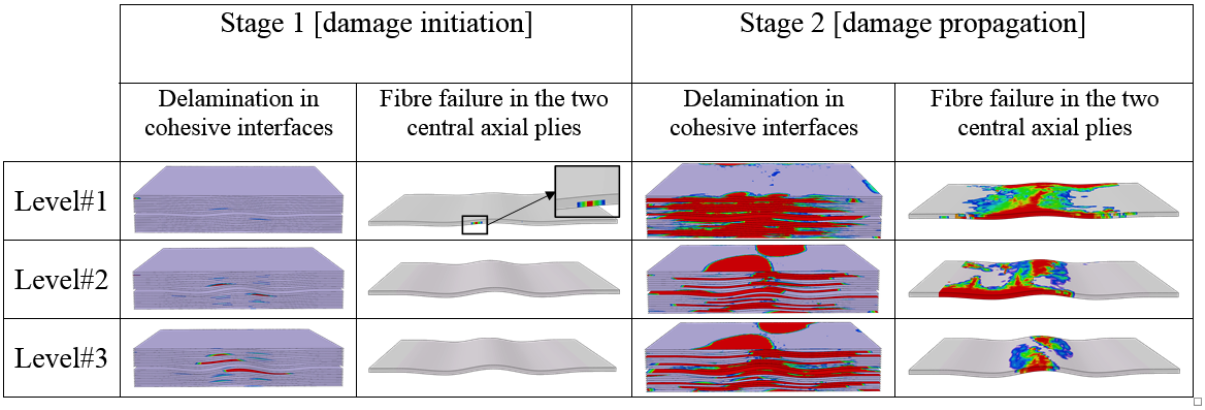

Figure 16. Damage initiation and progression in the three levels of wrinkle severities compared in regard to delamination and fibre failure. The elements in red in the contour map in each case are failed.

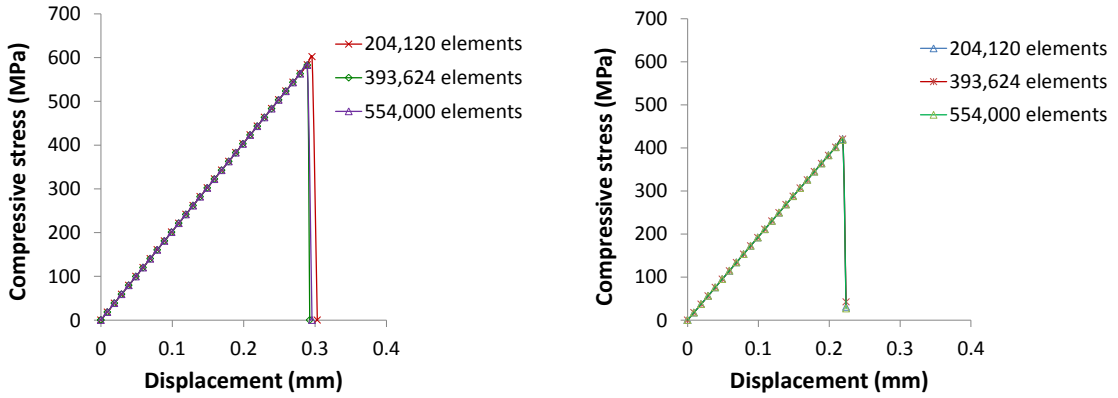

Figure 17. Mesh refinement studies for (a) model of level#1 wrinkle severity dominated by fibre failure. (b) model of level#3 wrinkle severity dominated by delamination.

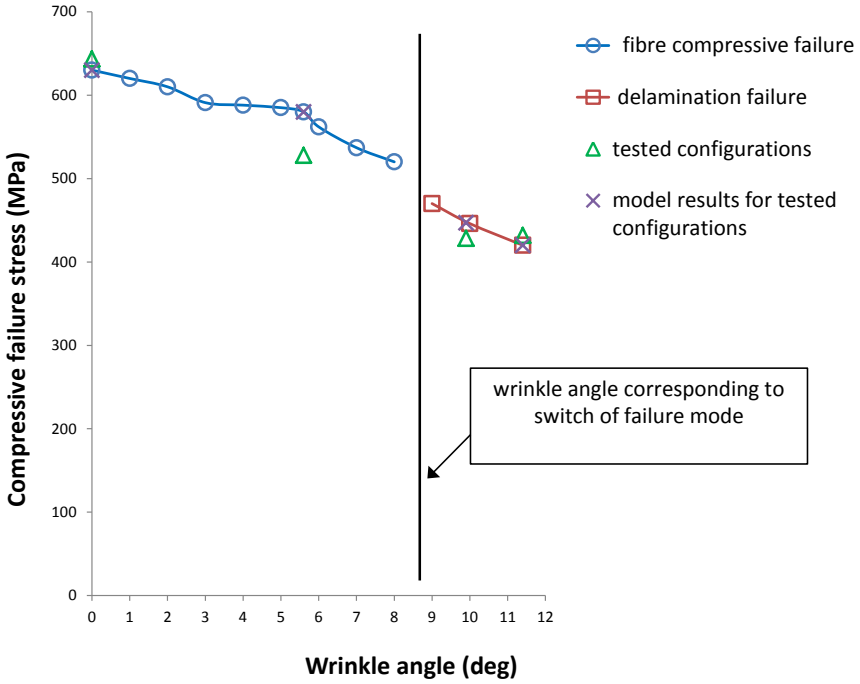

Figure 18. Wrinkle severity vs. compressive failure stress indicating a change of failure mode from fibre failure to delamination beyond a certain threshold severity.

Tables

Table 1. Undamaged thermo-elastic properties of IM7/8552 [23]

E_{11} (MPa)	E_{22} (MPa)	E_{33} (MPa)	γ_{12}	γ_{13}	γ_{23}	G_{12} (MPa)	G_{13} (MPa)	G_{23} (MPa)	α_{11} (/°C)	α_{22} (/°C)	α_{33} (/°C)
161000	11380	11380	0.32	0.32	0.43	5170	5170	3980	0	3e-5	3e-5

Table 2. IM7/8552 properties for matrix crack and fibre kink model[14,15,23]

Y_C (MPa)	S_L (MPa)	G_{Ic} (N/mm)	G_{IIc} (N/mm)	G_{kink} (N/mm)	α	θi (deg)
250	113	0.26	1.002	80	1	1.5

Table 3. IM7/8552 properties for the delamination model [23,24]

K_I (N/mm^3)	K_{II} (N/mm^3)	σ_{Imax} (MPa)	σ_{IImax} (MPa)	G_{Ic} (N/mm)	G_{IIc} (N/mm)	α
10^5	10^5	60	90	0.26	1.002	1

Table 4. Wrinkle compression test results

wrinkle severity	failure stress	
	mean (MPa)	CV (%)
pristine	643.5	6.3
level#1	527.9	5.2
level#2	428.4	4.9
level#3	432.0	6.9